Transverse permeability of roving-based fibrous media: Influence of resin rich layers

Yuksel, O.; Błazucki, S.K.; Broggi, G.C.; Caglar, Baris

Publication date
2023

Published in
Proceedings of the 23rd International Conference on Composite Materials (ICCM23)

Citation (APA)
Yuksel, O., Błazucki, S. K., Broggi, G. C., & Caglar, B. (2023). Transverse permeability of roving-based fibrous media: Influence of resin rich layers. In *Proceedings of the 23rd International Conference on Composite Materials (ICCM23)*

TRANSVERSE PERMEABILITY OF ROVING-BASED FIBROUS MEDIA: INFLUENCE OF RESIN RICH LAYERS

O. Yuksel[1], S. Blazucki[1], G. Broggi[2] and B. Caglar[*1]

[1] Department of Aerospace Structures and Materials, Faculty of Aerospace Engineering, Delft University of Technology, the Netherlands
[2] Laboratory for Processing of Advanced Composites (LPAC), Institute of Materials (IMX), Faculty of Engineering (STI), Ecole Polytechnique Federale de Lausanne (EPFL), Lausanne, Switzerland
*b.caglar@tudelft.nl

Keywords: Permeability, Liquid composite molding, Pultrusion, Anisotropy, Microstructure

ABSTRACT

Transverse permeability is a key parameter to construct accurate process modelling frameworks for composite manufacturing processes whereby dry reinforcements are impregnated by a resin. The transverse permeability of fibrous structures is strongly correlated with the spatial fiber distribution which is inevitably irregular through the cross section. This irregularity and possible resin channel formation through the cross section cause complex permeability field. In this study, we analysed the correlation between the microstructural features and the apparent transverse permeability. Multiple regions of interest were collected from a pultruded part's cross section that exhibited apparent resin rich layers. Apparent transverse permeability values of these Regions of Interest (ROIs) were calculated by using OpenFOAM. The principal components of the transverse were calculated, and the statistical descriptors were captured for the corresponding ROIs. The principal permeability component analysis showed that principal directions are in-line with the visual predictions. The correlation between the permeability components and the statistical descriptors shows some traces of the capability of predicting the transverse permeability and the principal components based on the microstructural features., A larger dataset and more elaborate statistical descriptors are needed for accurate prediction of the flow behaviour and the apparent permeability components.

1 INTRODUCTION

Numerical process simulations for liquid composite molding (LCM) processes are used for identifying the optimal process conditions, more specifically the optimum resin inlet and vacuum port locations for vacuum infusion, optimal inlet resin pressure, air vent locations, and temperature for resin transfer molding (RTM) [1], also for continuous processes optimal conditions, e.g., the resin injection pressure, pulling speed, and injection box design for resin injection pultrusion (RIP) [2,3]. The permeability characteristic of the fiber reinforcement is one of the key elements for these process simulations. However, the local variability in fiber distribution and the resin rich layers through the cross section result in a complex permeability field and necessitates the use of accurate models for permeability prediction that account for the microstructural variation.

In the present work, the relationship between the microstructural features and the transverse permeability of a fibrous media was investigated using microscale numerical flow simulations. Several regions of interest were collected from a pultruded part. These flow domains, containing irregularly distributed filaments and intra-tow regions, i.e., resin-rich layers, were transferred to the OpenFOAM simulations. Spatial fiber distribution within these ROIs was systematically analyzed utilizing commonly used statistical descriptors. The correlation between these descriptors and the calculated permeability values was further studied. Principal component analysis was performed to estimate the principal permeability components and the principal direction of the captured ROIs. A novel approach was proposed to express the microstructural anisotropy, and its correlation to the anisotropy of permeability was discussed for both the captured and the principal permeability values.

2 MATERIALS AND METHODS

2.1 Materials and sample preparation

The individual fiber locations and their diameter in the experimentally captured regions of interest (ROIs) were identified and were used for creating a meshed structure to be used in CFD simulations to evaluate the correlation between the microstructural features and the transverse permeability. The ROIs used in the simulations were collected from a 19.5×19.5 mm^2 square cross-section of a unidirectional glass fiber-reinforced polyester pultruded part.

A water-cooled diamond saw was used to cut the pultruded part, which is then embedded into cold mounting epoxy for the grinding/polishing steps. The 500, 1000, 2000, and 4000 grit size grinding papers and the proper polishing clothes with 9, 3, 1 µm solution were used for preparing the surface in an automated polishing machine 'Struers Tegramin-30'.

The micrographs of the polished cross-section were captured using an optical microscope, 'Keyence VHX 1000', with ring illumination. Images were taken with 400× magnification with automatic stitching. The entire cross-sectional area was bigger than the stitching limit of the microscope. Hence, in total, four stitched images were stitched manually to capture the entire cross-sectional area of 19.5×19.5 mm^2.

Each filament over the cross section was detected via image processing using a built-in circle finding function, 'imfindcircles', in Matlab (R2019b). The overlapped circles were identified and eliminated using an in-house algorithm. Reader is referred to reference [4] for the details of the preparation steps and the fiber volume fraction distribution over the corresponding cross section. The locations and radii of the filaments within the arbitrarily chosen ROIs were exported to create the flow domains. Square-shaped ROIs with three different edge lengths were collected from the corresponding cross-section. The investigated cross-sectional area and an example ROI for each edge length used in this study can be seen in Fig. 1.

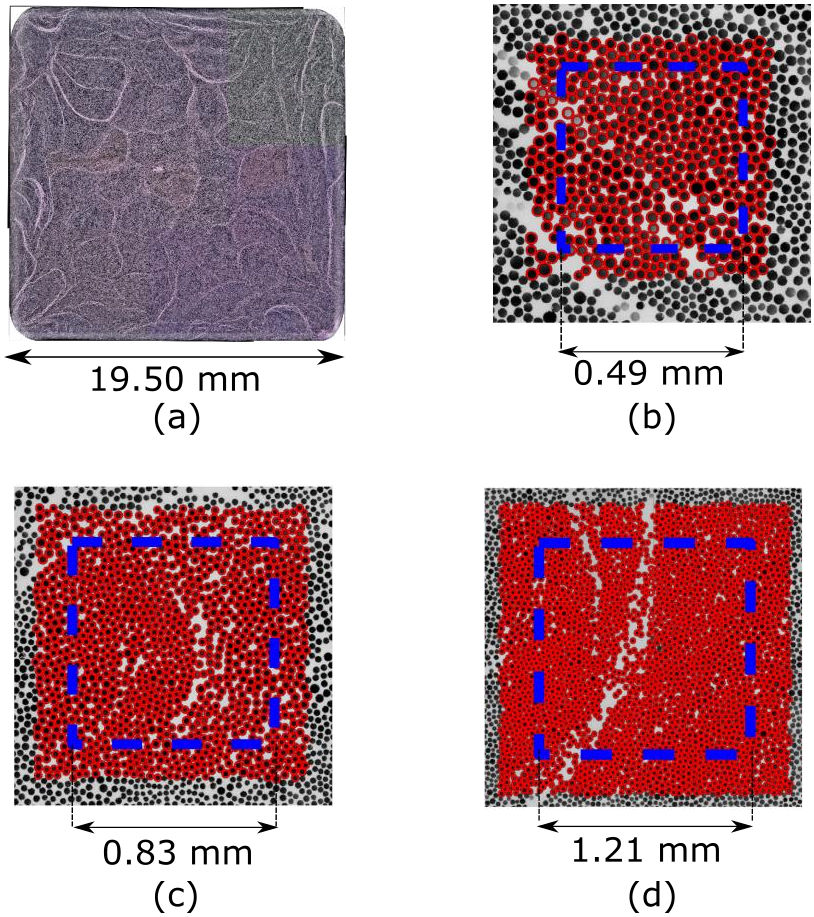

Figure 1: (a) The entire cross-section of the investigated pultruded part. The example ROIs for the used edge lengths; (b) 0.49 mm, (c) 0.81 mm, and (d) 1.21 mm.

2.2 Statistical fiber distribution analysis

To understand the relationship between the microstructural features and the transverse permeability, the fiber distribution within the investigated ROIs was systematically analyzed utilizing statistical descriptors. The nearest neighbor distances are some of the most commonly used descriptors in the composite materials community [5,6]. These statistical descriptors represent the distance between each filament and its first, second, third, etc., nearest neighbor filament, which can be presented as a distribution or used as just an average value. From a permeability perspective, the gap between closer filaments is more critical from the permeability perspective due to corresponding to the channels' width between the neighbor filaments [7]. To this end, the distance between fiber walls was used in this study to overcome the limitation of the center-to-center distance based approaches when the fibers' diameter vary significantly as is our case, as visualized in Figure 1.

Another common descriptor to assess the fiber distribution is based on Voronoi tessellation to divide the cross-sectional area into polygons assigned to individual filaments. The points within each polygon have no closer filament than the assigned filament. The fiber volume fraction of these polygons is a useful measure to represent the local fiber volume fraction distribution. This distribution or the standard deviation of the local V_f values, therefore, reveals the non-uniformity of fiber distribution over the investigated cross sections.

The descriptors explained above represent a quantitative measure for the local spatial fiber distribution or the uniformity of the microstructure. However, they do not provide any insight into the directional formation or connectivity of the porous channels between highly packed fiber clusters. Herein we propose a new statistical descriptor to evaluate the connected channels and their directionality. The linear densities of fibers on both horizontal and vertical lines were calculated through

the acquired ROIs. Each ROI was binarized as a window of 400×400 pixels. The pixels in fibers were given a value of 1, and all the remaining pixels were given a value of 0. Fig. 2 (d) shows an ROI and schematic representation of linear fiber density profiles. The upper sub-plot in Fig. 2 (d) shows the linear fiber density values in vertical lines along the X axis, while the right sub-plot shows the linear fiber density values in horizontal lines along the Y axis. The following equation (eq. 1) shows the mathematical expression of the standard deviation ratio of linear fiber densities.

$$S = \frac{\sqrt{{}^{1}\!/_{400}\sum_{x=0}^{400}\left(\sum_{y=0}^{400}P(x,y)-\Theta\right)^{2}}}{\sqrt{{}^{1}\!/_{400}\sum_{y=0}^{400}\left(\sum_{x=0}^{400}P(x,y)-\Theta\right)^{2}}} \tag{1}$$

where, P is the pixel value 1 or 0. The areal fraction of pixels within fibers to the total ROI area is Θ. The term, Θ, is used both in nominator and denominator to make it simpler, as it is equal to both the average of linear fiber densities in vertical lines and the average of linear fiber densities in horizontal lines. The variable, S, is the standard deviation ratio of linear fiber densities.

3 OPENFOAM SIMULATIONS

In an attempt to gain insight into the relationship between the microstructural features and the anisotropic transverse permeability, we performed CFD simulations using the C++ based open-source toolbox OpenFOAM 7 [8] to derive ROIs' permeability in transverse directions. Modeling steps were wrapped with a Python script built on the PyFoam library [9] for automation purposes.

Fiber centers and radii data of the captured ROIs were fed into the model and meshed with BlockMesh and SnappyHexMesh utilities included in OpenFOAM. The former was used do generate a regular mesh which was then snapped over the fibers with the latter. As SnappyHexMesh requires a 3D mesh to work properly, the extrudeMesh utility was used to generate a one-layer 2D mesh by extruding one slice from its output. An adaptive meshing algorithm was implemented to refine the mesh in the vicinity of the fibers to ensure that channels between closely packed fibers were meshed properly. The mesh sensitivity was analyzed to identify the best compromise between mesh size and mesh independence of the results. Moreover, mesh refinement levels and the model were validated against analytical solutions of Gebart's transverse permeability model for rectangular and hexagonal packings.

ROIs' edges perpendicular to the overall flow direction were set as inlet and outlet patches. Fixed pressures Pin and Pout were then applied to them, as illustrated in Fig. 3. The velocity field was constrained with a zero-gradient condition. ROIs were not periodic and symmetrical conditions were found to artificially increase permeability by implicitly creating flow channels. A 15 μm outlet region was added to allow for outlet flow homogenization, following the strategy used in reference [10]. Symmetrical boundary conditions were applied to the edges tangential to the flow, and remaining patches were set as empty.

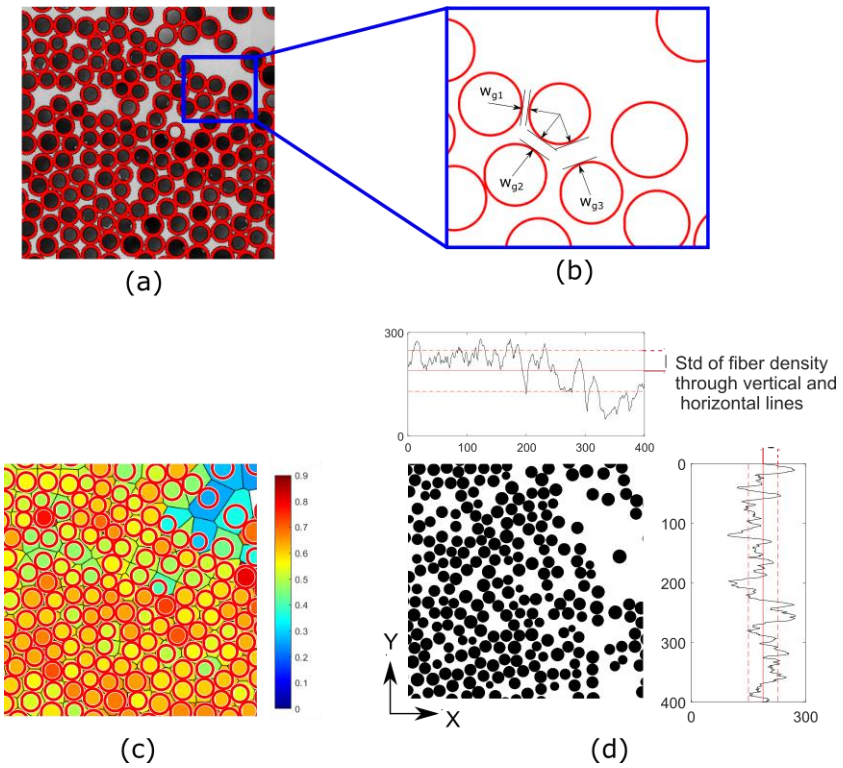

Figure 2: (a) Detected fibers, (b) representation of the 1st, 2nd, and 3rd nearest neighbor, (c) Voronoi tessellation with the colormap of local fiber volume fraction, and (d) schematic representation of the standard deviation of the linear fiber densities

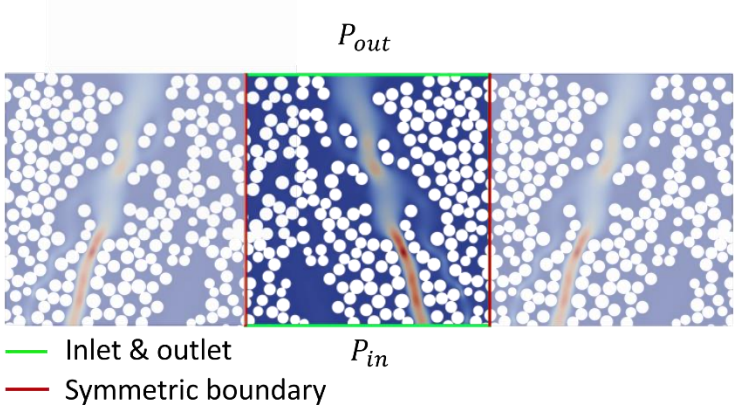

Figure 3: Visualization of an ROI with the boundary conditions.

The model fluid was assumed to be incompressible, and the flow was assumed to be in a steady state, which means that permeability could be derived according to Darcy's Law. As permeability depends only on the geometrical parameters [11], an arbitrary pressure gradient, ΔP, of 1 bar was applied between the inlet and outlet. It was chosen to ensure a low Reynolds number and, thus, a creeping flow. This assumption was verified a posteriori by evaluating the Reynolds number in critical areas. Most of the values were found to be typically two to three orders of magnitude below 1, which validates an overall creeping flow. The corresponding velocity field was determined with the SimpleFoam solver, which uses the SIMPLE (Semi-Implicit Method for Pressure Linked Equations) method [12] to solve the coupled Navier-Stokes equations, i.e., the continuity equation and the momentum conservation equation. For a creeping flow with constant density and viscosity, they read as in Eq. 2 and Eq. 3, respectively.

$$\nabla \cdot u = 0, \tag{2}$$

$$\partial u / \partial t + (u \cdot \nabla) u = \nu \nabla^2 u - \nabla p \tag{3}$$

where u is the flow velocity, p is the pressure and $\boldsymbol{\nu}$ ($= {}^{\mu}/_{\boldsymbol{\rho}}$) is the kinematic viscosity. It should be noted that the time derivative is null, as the solver was used in a steady-state configuration. Typical epoxy values of $\rho = 1.25$ [g· cm^{-3}] and $\mu = 0.5$ [Pa· s] were used, after which the output flow rate Q can be determined with the flowRatePatch function to derive the permeability.

3.1 Determining principal permeability components in the transverse plane

As briefly explained in the introduction, the existence of resin-rich layers, i.e., continuously formed larger gaps between fibers, may contradict the assumption of a transversely isotropic permeability field for UD-reinforced composites. These resin-rich layers behave like low flow resistant channels, which results in higher transverse permeability along their directions. To investigate the influence of these resin rich layers together with inevitable microstructural irregularities, the principal components of 2D transverse permeability should be determined.

Three unidirectional flow experiments carried out along three different in-plane directions, are sufficient to derive the principal permeability components in 2D [13]. The captured ROIs were rotated for this purpose, and the OpenFOAM simulations were run through these rotated ROIs as one-directional flow experiments. Fig. 4 shows an ROI and its rotated counterparts. The following equations were used to calculate the principal components of the permeability and the principal direction.

$$\beta = \frac{1}{2}\tan^{-1}\left(\frac{A}{D} - \frac{A^2 - D^2}{K_{II}\cdot \boldsymbol{D}}\right), \tag{4}$$

$$K_1 = K_I\left(\frac{A-D}{A-{}^{D}/_{cos2\beta}}\right), \tag{5}$$

$$K_2 = K_{III}\left(\frac{A+D}{A+{}^{D}/_{cos2\beta}}\right). \tag{6}$$

where, $\boldsymbol{A} = \left(\frac{\boldsymbol{K_I + K_{III}}}{\boldsymbol{2}}\right)$ and $\boldsymbol{D} = \left(\frac{\boldsymbol{K_I - K_{III}}}{\boldsymbol{2}}\right)$.

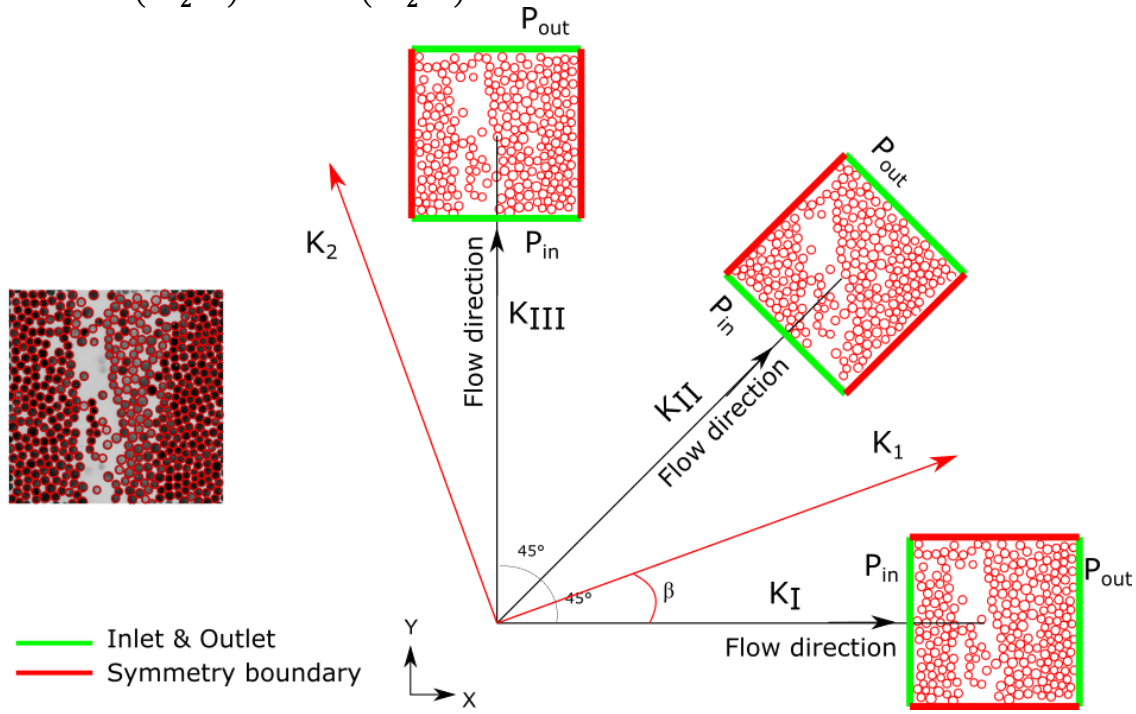

Figure 4: Schematic representation of the three directions for the 1D flow simulations to derive the principal direction and the principal permeability components.

4 RESULTS AND DISCUSSION

Fig. 5 shows the apparent permeability results of each ROI in X- and Y-directions. Flow simulations were carried out using 39 ROIs with an edge length of 0.49 mm, 13 ROIs with an edge length of 0.83 mm, and 9 ROIs with an edge length of 1.21 mm. These regions were captured over the entire cross-section with equal spacing to avoid selection of preferential locations. In the investigated pultruded part, there is a fiber volume fraction gradient over the cross section, such as lower fiber content in the center of the part and higher fiber content in the outer regions. This phenomenon facilitates a larger fiber volume content range within the captured ROIs. The variabililty in the fiber volume fraction decreases with increasing edge length and well within the range that is relevant for advanced composites.

Fig. 5 (a) presents the OpenFOAM results together with the Gebart's analytical model for the hexagonal distribution [14]. The average fiber radius in the investigated pultruded part is 14.5 µm which was used for the Gebart's solution. In parallel with the observations made in the literature [15], Gebart's model gives the upper bound for the numerically estimated transverse permeability results except for the couple of ROIs which have apparent resin rich channels. Fig. 5 (b) shows that there is an anisotropy of the transverse permeability components without a preferential direction. This can be attributed to the characteristics of the pultrusion process and the investigated cross section.

Fig. 6 (a) shows the numerical permeability results (KI, KII, KIII) together with the principal permeability components calculated using eq. 4, eq. 5, and eq. 6. For the sake of clarity, the principal component analysis was only performed for the ROIs with 0.49 mm edge length. As it can be seen in Fig. 6 (a), the principal permeability components provide the upper and the lower bounds for each ROI. While the lower principal permeability components are all well below the Gebart's model, some of the higher principal components are above the Gebart's model. It was observed that the ROIs with higher principal permeability components than the Gebart's model have visible resin rich channels in them. The ROIs shown in Fig. 6 (b) and (d) can be good examples of these ROIs having resin rich regions and principal components higher than Gebart's model. It is worth noting that the rotated ROIs used in the simulations for K_{II} (in Fig. 4) is not exactly same with the ROIs used for K_I and K_{III} due to the corner regions. The overall fiber volume content for the ROIs used for K_{II} might be slightly different than its counterparts and the open channels in some of the ROIs might get blocked in the rotated versions. In these scenarios, it is possible to over- or under-estimate the principal permeability components. Therefore, future work will focus on checking the estimated principal components with simulations run through the principal directions. For the currently available results, though, the estimated values can be considered reasonable and the principal directions are well aligned with the visible resin rich regions.

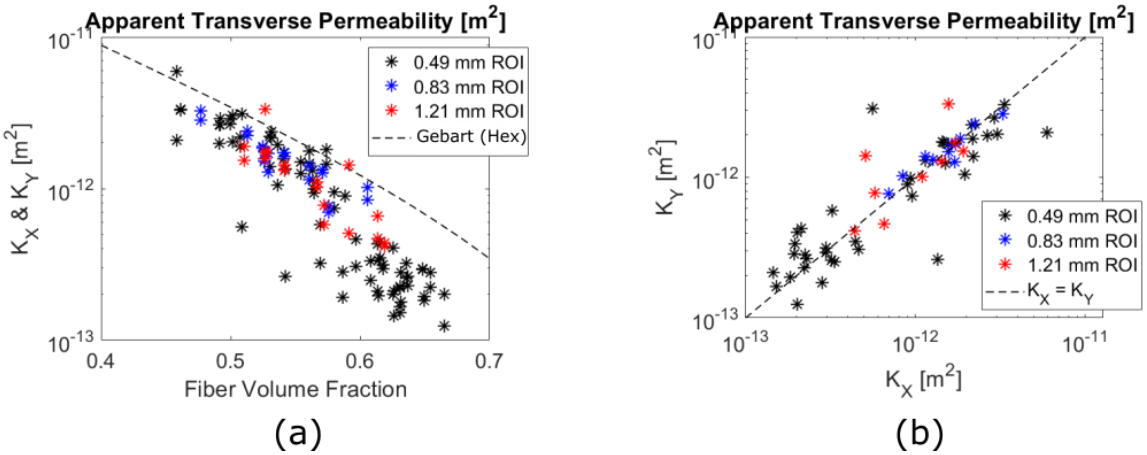

Figure 5: Apparent transverse permeability values for each ROI; (a) K_X and K_Y vs. fiber volume fraction, (b) K_Y vs. K_X.

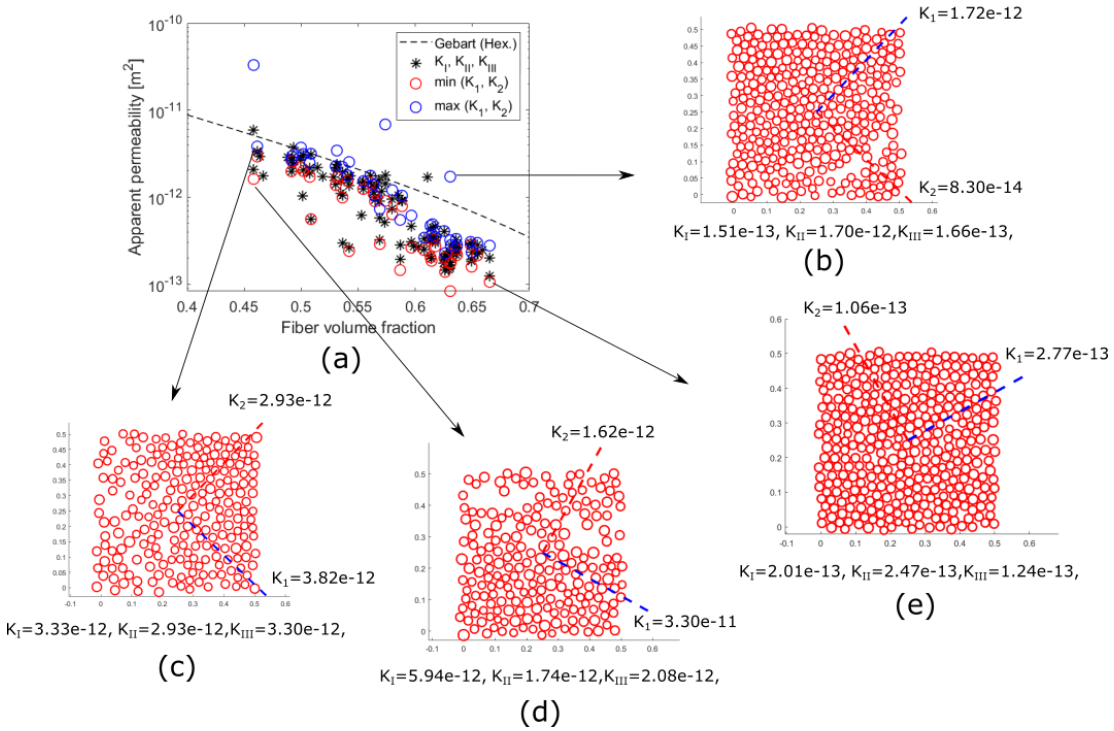

Figure 6: (a) Principal transverse permeability components. (b, c, d, e) Some representative ROIs with the numerical results, the calculated principal components, and the corresponding principal directions.

The correlation between the first, second, and third nearest neighbor distances with the lower principal permeability component is shown in Fig. 7 (a). The fiber volume fraction values of the corresponding ROIs are also indicated by a colormap in this figure. In general, the nearest neighbor distances increase with decreasing fiber volume fraction. However, the difference between the first, second , and third neighbor distances is proportional to the fiber volume fraction. This can be commented as a consequence of increasing uniformity. Another statistical descriptor representing the overall uniformity of fiber distribution is the standard deviation of the Voronoi cells' fiber volume fraction values. The correlation between standard deviation of local fiber volume fraction values and the minimum principal permeability component is shown in Fig. 7 (b). The observation of increasing fiber distribution uniformity with decreasing fiber volume fraction is also confirmed by this correlation. As a general trend, the investigated statistical descriptors show a linear dependency to the minimum principal permeability component. Results for the higher fiber content ROIs show relatively higher scatter. This might be caused by some microstructural features which are influential on the apparent permeability but not so visible with the chosen statistical descriptors.

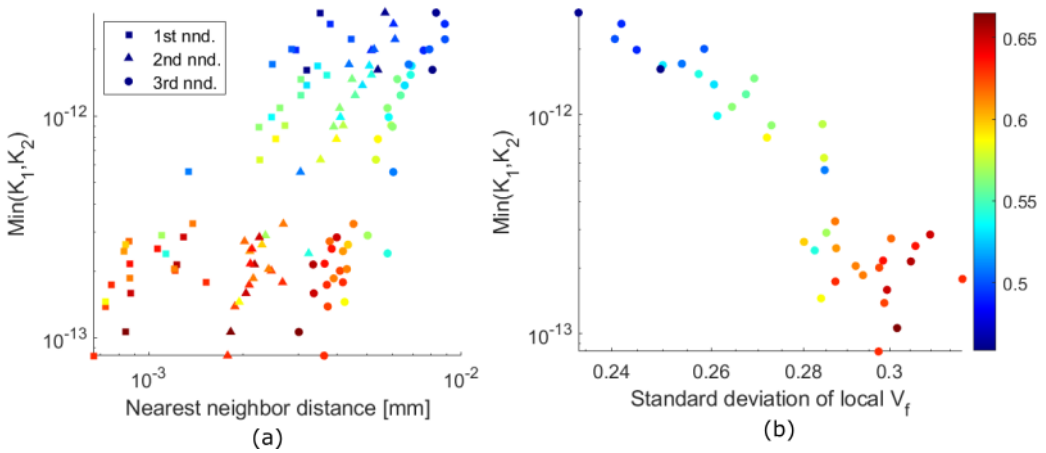

Figure 7: (a) The correlation between the average nearest neighbor distance and the minimum principal transverse permeability component ('nnd.' stands for the nearest neighbor distance). (b) The correlation between the standard deviation of local fiber volume fraction based on Voronoi tessellation and the minimum principal transverse permeability component. Color bar shows the corresponding fiber volume fraction values.

Fig. 8 presents the correlation between the permeability anisotropy and the standard deviation ratio of the linear fiber densities (eq. 1). The measured permeability values show relatively linear correlation to the standard deviation ratio. Considering the fiber volume fractions, it can be commented as the ROIs with relatively higher fiber volume fraction have a lower standard deviation ratio and anisotropy too. For the lower range of the fiber volume fractions, some of the ROIs' standard deviation ratio is nicely correlated with the anisotropy in transverse permeability. Most of the data points accumulate around the standard deviation ratio of 1 and do not have a strong anisotropy which can be attributed to the randomly distributed intra-tow regions through the cross section. Ratio of the principal permeability components, on the other hand, theoretically show the maximum possible anisotropy for each ROI. It can be said that there is a correlation between the standard deviation ratio captured for the principal directions and the anisotropy of the principal permeability components too. However, the results are more scattered for the principal components.

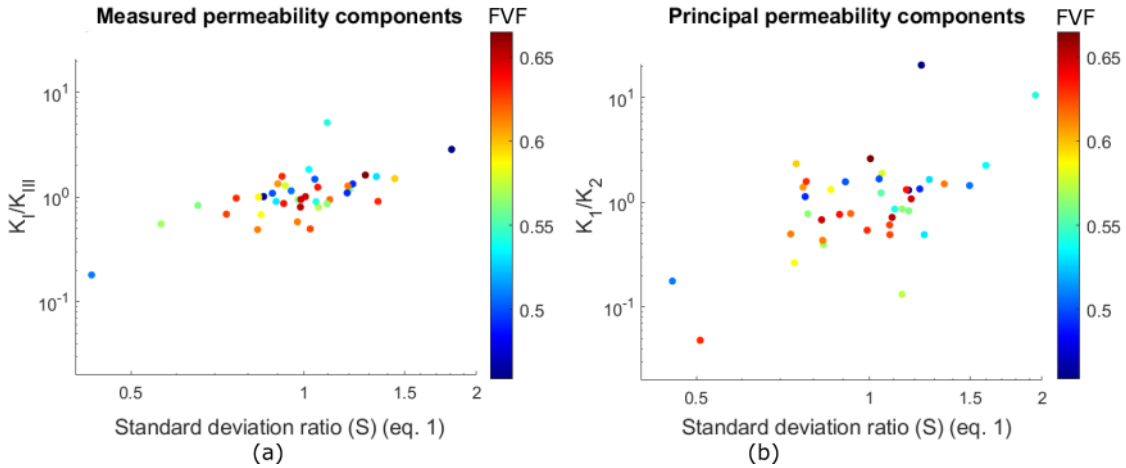

Figure 8: Transverse permeability anisotropy vs. standard deviation ratio (S); the measured components (a), and the principal components (b). Color bars show fiber volume fraction.

9 CONCLUSIONS

We investigated the microscale transverse permeability of realistic 2D microstructures by using numerical flow simulations in OpenFOAM. The analyzed statistical descriptors showed promisingly strong correlations to the transverse permeability values and furtherinvestigation using different descriptors is recommended. Principal component analysis provided reasonable estimation for the principal permeability component and the principal direction. In this study, the focus was on on the correlations between the descriptors and the apparent permeability, however, it is a combined effect of multiple descriptors which will be investigated in future work. Ultimately, deep learning based methods are expected to be useful to reveal the relationship between the microstructural features and the apparent permeability as demonstrated in [16].

REFERENCES

[1] E.M. Sozer, P. Simacek, S.G. Advani, Resin transfer molding (RTM) in polymer matrix composites, Resin transfer molding (RTM) in polymer matrix composites. Woodhead Publishing, pp. 245-309, 2012.

[2] M. Sandberg, O. Yuksel, I. Baran, J. H. Hattel, J. Spangenberg. "Numerical and experimental analysis of resin-flow, heat-transfer, and cure in a resin-injection pultrusion process". Composites Part B: Engineering, Vol. 143, 2021.

[3] Maximilian Volk, Onur Yuksel, Ismet Baran, Jesper H. Hattel, Jon Spangenberg, Michael Sandberg, Cost-efficient, automated, and sustainable composite profile manufacture: A review of the state of the art, innovations, and future of pultrusion technologies, *Composites Part B: Engineering*, **246**, 2022, 110135 (doi.org/10.1016/j.compositesb.2022.110135).

[4] O. Yuksel, M. Sandberg, J.H. Hattel, R. Akkerman, I. Baran, Mesoscale process modeling of a thick pultruded composite with variability in fiber volume fraction. *Materials*, **14(13)**, 2021, pp. 3763 (doi.org/10.3390/ma14133763).

[5] V. Romanov, S.V. Lomov, Y. Swolfs, S. Orlova, L. Gorbatikh, I. Verpoest, Statistical analysis of real and simulated fibre arrangements in unidirectional composites, *Composites Science and Technology*, **87**, 2013, pp. 126-134 (doi.org/10.1016/j.compscitech.2013.07.030)

[6] A.R. Melro, P.P. Camanho, S.T. Pinho, Generation of random distribution of fibres in long-fibre reinforced composites, *Composites Science and Technology*, **68**, 2008, pp. 2092-2102 (doi.org/10.1016/j.compscitech.2008.03.013).

[7] F. Gommer, A Endruweit and A.C. Long, Influence of the micro-structure on saturated transverse flow in fibre arrays, *Journal of Composite Materials*, **52(18)**, 2018, pp. 2463-2475 (doi: 10.1177/0021998317747954).

[8] H.G. Weller, G. Tabor, H. Jasak, C. Fureby, A tensorial approach to computational continuum mechanics using object-oriented techniques. *Computers in Physics* **12(6)**, 1998, pp. 620–631.

[9] B. Gschaider, M. Beaudoin,F. Pollesb¨ock, E. Lorriaux, B. Santos, M. Immer, et al. Pyfoam 2021.6. http://https://pypi.org/project/PyFoam//; 2021.

[10] O. Rimmel, D. May, Modeling transverse micro flow in dry fiber placement preforms. *Journal of Composite Materials*, **54(13)**, 2020, pp. 1691–1703. (doi.org/10.1177/0021998319884612)

[11] M. Bodaghi, G. Catalanotti, N. Correia, On the statistics of transverse permeability of randomly distributed fibers, *Composite Structures*, **158**, 2016 pp. 323-332 (doi.org/10.1016/j.compstruct.2016.09.045).

[12] L.S. Caretto, A.D. Gosman, S.V. Patankar, D.B. Spalding, Two calculation procedures for steady, three-dimensional flows with recirculation. In: Cabannes, H., Temam, R., editors. Proceedings of the Third International Conference on Numerical Methods in Fluid Mechanics. Berlin, Heidelberg: Springer Berlin Heidelberg. 1973, pp. 60–68. ISBN 978-3-540-38392-5

[13] A. Raizada, K.M. Pillai, P. Ghosh, A validation of Whitaker's closure formulation based method for estimating flow permeability in anisotropic porous media, *Composites Part A: Applied Science and Manufacturing*, **156**, 2022, pp. 106831 (doi.org/10.1016/j.compositesa.2022.106831).

[14] B.R. Gebart, Permeability of Unidirectional Reinforcements for RTM, *Journal of Composite Materials*, **26(8)**, 1992, pp. 1100-1133 (doi:10.1177/002199839202600802).

[15] E. Syerko, T. Schmidt, D. May, C. Binetruy, S.G. Advani, S. Lomov, L. Silva, S. Abaimov, N. Aissa, I. Akhatov, M. Ali, N. Asiaban, G. Broggi, J. Bruchon, B. Caglar, H. Digonnet, J. Dittmann, S. Drapier, A. Endruweit, A. Guilloux, R. Kandinskii, A. Leygue, B. Mahato, P. Martínez-Lera, M. Matveev, V. Michaud, P. Middendorf, N. Moulin, L. Orgéas, C.H. Park, S. Rief, M. Rouhi, I. Sergeichev, M. Shakoor, O. Shishkina, Y. Swolfs, M. Tahani, R. Umer, K. Vanclooster, R. Vorobyev, Benchmark exercise on image-based permeability determination of engineering textiles: Microscale predictions, *Composites Part A: Applied Science and Manufacturing*, **167**, 2023, pp. 107397 (doi.org/10.1016/j.compositesa.2022.107397).

[16] B. Caglar, G. Broggi, M.A. Ali, Laurent Orgéas, Véronique Michaud, Deep learning accelerated prediction of the permeability of fibrous microstructures, *Composites Part A: Applied Science and Manufacturing*, **158**, 2022, pp. 106973 (doi.org/10.1016/j.compositesa.2022.106973).